Research Square

Preprints are preliminary reports that have not undergone peer review.
They should not be considered conclusive, used to inform clinical practice,
or referenced by the media as validated information.

Vapor-liquid-solid epitaxy of wafer-scale perovskite single crystals

Guifu Zou

zougf3@mail.sysu.edu.cn

Sun Yat-sen University https://orcid.org/0000-0002-8342-7768

Yuan Chen

College of Mechanical and Electronic Engineering, Shandong University of Science and Technology

Guijia Hu

College of Mechanical and Electronic Engineering, Shandong University of Science and Technology

Jianmei Chen

Nanjing University of Posts & Telecommunications

Wei Zhang

College of Mechanical and Electronic Engineering, Shandong University of Science and Technology

Yongshu Wang

College of Mechanical and Electronic Engineering, Shandong University of Science and Technology

Hongcao Shi

College of Mechanical and Electronic Engineering, Shandong University of Science and Technology

Jinchuan Cao

College of Mechanical and Electronic Engineering, Shandong University of Science and Technology

Guoxiang Zhao

School of Energy, Soochow University

Chen Wang

School of Energy, Soochow University

Peipei Ma

School of Energy, Soochow University

Hao Wang

Nanjing University https://orcid.org/0000-0002-3548-7870

Shan Cong

School of Energy, Soochow University

Article

Keywords:

Posted Date: October 14th, 2026

DOI: https://doi.org/10.21203/rs.3.rs-11177182/v1

License: This work is licensed under a Creative Commons Attribution 4.0 International License.
Read Full License

Additional Declarations: There is **NO** Competing Interest.

Abstract

Wafer-scale halide perovskite single-crystal films are highly sought after for integrated optoelectronic applications. However, conventional vapor-phase growth suffers from poor substrate wettability and restricted precursor diffusion, consequences of the high interfacial energies inherent to vapor-solid interfaces at both the vapor-substrate and vapor-film boundaries. Here, we report catalyst-free vapor–liquid–solid (VLS) growth of 2-inch perovskite single-crystal wafers. This process is mediated by a condensed halide-rich liquid intermediate that establishes complete surface wetting and replaces high-energy vapor–solid interfaces with low-energy liquid–solid interfaces, thereby substantially reducing the nucleation energy barrier and nucleation density. The liquid-phase medium also dramatically extends metal halide solute migration distances, enabling edge-dominated layer growth and seamless coalescence of oriented nuclei. We demonstrate the generality of this approach by fabricating wafer-scale films of $CsPbBr_3$, $CsPbCl_3$, and their alloys. Atomic-scale microscopy and wafer-scale spectroscopy confirm exceptional crystalline uniformity, ultralow trap-state density, and superior electronic and optoelectronic quality.

Introduction

Metal halide perovskites have demonstrated remarkable performance across diverse optoelectronic applications, including solar cells,[1–3] light-emitting diodes (LEDs),[4–6] laser diodes,[7–8] and visible light /radiation detection.[9–12] However, polycrystalline perovskite films suffer from abundant grain boundaries that induce carrier scattering, Joule heating, and ion migration, severely compromising device efficiency and long-term stability.[13–14] In contrast, single-crystal perovskites represent ideal building blocks for high-performance optoelectronic devices.[15–16] Single-crystal perovskite solar cells and LEDs have already achieved benchmark efficiency and stability metrics.[17–19] Yet practical device integration and mass fabrication require scalable synthesis of large-area single-crystal perovskite wafers.[20–23] Several strategies—including solution space confinement,[24–26] and solution- or vapor-phase epitaxy[27–30] have been explored, but wafer-sized single-crystal perovskite growth remains a critical bottleneck.[30–31]

Conventional chemical vapor deposition (CVD) for perovskite epitaxial growth relies critically on substrate wettability and vapor-phase diffusion characteristics.[32] Highly lattice-matched single-crystal substrates with low surface energy—including mica, sapphire, NaCl, GaN, $SrTiO_3$, KCl, and ZnSe—have been validated for epitaxial deposition of single-crystal perovskites.[29–31, 33–36] However, vapor-phase growth of large-area single-crystal thin films faces a fundamental thermodynamic-kinetic dilemma arising from high-energy vapor–substrate and vapor–film interfaces, which promote the formation of numerous three-dimensional (3D) islands and prevent their coalescence into continuous single crystals.[37] This challenge is further amplified by heterogeneous nucleation, gas-phase pre-reactions, and flow-field nonuniformities. Consequently, large-scale growth suffers from random, explosive nucleation; nonuniform domain coalescence; and film discontinuity across substrates.

Here, we report catalyst-free VLS growth of 2-inch perovskite single-crystal wafers mediated by a condensed halide-rich liquid intermediate. This intermediate creates complete surface wetting and replaces high-energy vapor–solid interfaces with low-energy vapor–liquid and liquid–solid interfaces, substantially reducing both the nucleation energy barrier and nucleation density. The liquid-phase medium also dramatically extends metal halide solute migration distances, enabling edge-dominated layer growth and seamless coalescence of oriented nuclei. We demonstrate the versatility of this approach by fabricating wafer-scale films of $CsPbBr_3$, $CsPbCl_3$, and their alloys. Atomic-scale microscopy and wafer-scale spectroscopy confirm exceptional crystalline uniformity, ultralow trap-state density, and superior electronic and optoelectronic performance.

Results and discussions

Characterization of perovskite single-crystal wafer

All-inorganic halide perovskite $CsPbBr_3$ single-crystal films with 2-inch diameters were grown on both sapphire and mica substrates, exhibiting excellent continuity and full substrate coverage (Fig. 1a, Supplementary Fig. S1). Cross-sectional imaging reveals a uniform, dense 1.63-μm-thick film free of grain boundaries; the $CsPbBr_3$/sapphire interface exhibits intimate contact, indicative of robust van der Waals epitaxial coupling (Fig. S2a). Optical microscopy shows a compact, smooth surface free of islands, cracks, or uncovered regions, confirming the high surface quality of the single-crystal wafers (Supplementary Fig. S2b). Atomic force microscopy (AFM) further verified surface quality, revealing atomically smooth topography with a root-mean-square roughness of 0.94 nm over a 10 × 10 μm² area (Supplementary Fig. S3)—a critical attribute for optimized device interfaces.

The chemical composition and microstructure of as-grown $CsPbBr_3$ films were comprehensively characterized. Out-of-plane X-ray diffraction (XRD) presents two sharp peaks indexed to the (001) and (002) planes of cubic $CsPbBr_3$, demonstrating preferential [00*l*] crystallographic orientation (Supplementary Fig. S4a). In-plane XRD φ-scans of the (101) reflection over − 180° to 180° display fourfold-symmetric peaks with uniform spacing, consistent with the cubic crystal structure (Fig. 1b). The full-width at half-maximum (FWHM) of the φ-scan peaks is 0.63°, indicating strong epitaxial alignment between the perovskite film and substrate. The ω-scan rocking curve of the main diffraction peak exhibits a sharp profile with an FWHM of 0.01° (Supplementary Fig. S4b), indicative of exceptional crystalline quality and ultralow defect density.

Electron backscatter diffraction (EBSD) was employed to map crystallographic orientation across the $CsPbBr_3$ wafer. Pole figures for the [001], [101], and [111] directions all present well-defined spot-like projections (Supplementary Fig. S5). EBSD maps of crystal domain boundaries show consistent orientation in both (001) and (100) planes, ensuring overall orientational uniformity after coalescence (Supplementary Fig. S6). Moreover, measurements across 15 distinct regions (labeled in Fig. 1a) and photoluminescence (PL) maps across the full 2-inch film confirm consistent (001) orientation and uniform emission throughout the wafer (Fig. 1c, h).

Scanning transmission electron microscopy (STEM) was performed on focused ion beam (FIB)-milled lamellae to resolve atomic-scale microstructure. High-resolution STEM images reveal highly ordered atomic arrangements in the $CsPbBr_3$ film (Fig. 1d), with a well-defined, abrupt $CsPbBr_3$/sapphire interface that further corroborates the epitaxial interaction. Fast Fourier transform (FFT) patterns of the entire STEM field of view show well-resolved lattice dots (Fig. 1e); the (110) and (002) lattice planes of $CsPbBr_3$ are clearly identified, confirming the single-crystalline nature. Diffraction spots from the Al_2O_3 substrate (marked with a red ring) are also resolved and indexed to the (001) plane, verifying that $CsPbBr_3$ (110) is epitaxially matched to c-plane sapphire (001). Lattice spacings of 5.6 Å and 7.93 Å in vertical and horizontal directions correspond to the (001) and (110) planes from Cs and Br atomic columns, respectively (Supplementary Fig. S7).

VLS growth occurred preferentially at higher temperatures and lower pressures (Fig. 1g), where precursors more readily evaporate and condense into the liquid phase. Film thickness depends on reaction time (Supplementary Fig. S8), with growth rate fitted to a mono-exponential function, enabling film thicknesses from 0.5 to 15 μm in our experiments. Moreover, these 2-inch wafer-scale single crystals represent a substantial advance over state-of-the-art synthetic approaches (Fig. 1f).[18–19, 26–27, 29–31, 36, 38–39] Collectively, these characterizations confirm successful growth of all-inorganic $CsPbBr_3$ single-crystal epitaxial wafers with exceptional crystallinity, uniform orientation, and wafer-scale homogeneity.

VLS epitaxy process for growing perovskite single crystals

The VLS process for growing $CsPbBr_3$ single-crystal wafers is illustrated in Fig. 2a. CsBr and $PbBr_2$ powders were uniformly mixed and loaded into an alumina crucible placed at the center of a tube furnace, with the substrate positioned to fully cover the crucible opening. The furnace was subsequently heated to a fixed temperature (e.g., 510°C) and held. As the precursor mixture gradually evaporated, precursor vapor condensed on the substrate to initiate nucleation and subsequent growth (Fig. 2b, c), ultimately yielding a uniform, continuous $CsPbBr_3$ single-crystal film conformally deposited across the entire substrate surface. Full substrate coverage of the crucible not only creates a uniform heating zone but also ensures homogeneous vapor diffusion geometry. No carrier gas was used during growth; instead, vacuum conditions eliminated airflow-induced vapor-phase disturbances and ensured stable, continuous precursor diffusion to the substrate.

To elucidate the intrinsic mechanism underlying the VLS method, growth features were investigated in detail using in situ visual CVD technology, which enables real-time observation of dynamic crystallization by simulating vapor-phase conditions and monitoring temporal evolution through optical imaging.[40] Initially, crystals observed via optical microscopy presented irregular shapes with curved edges. Upon holding at the growth temperature for tens of seconds, lateral dimensions gradually increased (Fig. 2d, Supplementary Video S1). Notably, as crystals grew, their irregular morphology was retained, with

regions of larger edge curvature growing faster than those with lower curvature—indicating no crystallographic plane dependence.

Statistical analysis of domain size evolution over time showed an increase of approximately 3,200 μm² within 4 minutes (Fig. 2e), fitting well with a quadratic time dependence (R^2 = 0.999, $D \sim t^2$). Moreover, length changes along horizontal (X) and vertical (Y) directions were recorded and analyzed, revealing nearly uniform edge growth without obvious anisotropy (Fig. 2f). From linear fit slopes, growth rates were determined to be 0.138 and 0.155 μm s^{-1} for horizontal and vertical directions, respectively. Substrate coverage over time was also examined (Fig. 2g), revealing a well-fitted quadratic dependence (R^2 = 0.998) described by:

$A \sim t^2$ (1)

This relationship arises because film coverage is proportional to the total area of all single-crystal domains on the substrate surface, and individual domain coverage is proportional to the square of growth time. Therefore, total coverage can be expressed as:

$A = \sum_i A_i \sim t^2$ (2)

Where t_i represents the nucleation time of newly formed nuclei during growth. Neglecting contributions from new nuclei, Equations (1) and (2) are equivalent. This relationship indicates stable, continuous, and uniform single-crystal film growth—a critical prerequisite for fabricating large-scale wafers.

Additionally, during film growth, a liquid-phase region several micrometers wide was consistently present at crystal edges (marked in Fig. 2d). This observation suggests that film growth follows a VLS mechanism, where vapor first condenses into droplets at crystal edges, followed by film crystallization driven by liquid-to-solid phase transition. The VLS growth mode is typically associated with synthesis of one-dimensional perovskite wires using metal nanoparticle catalysts (e.g., Sn, Pb).[41–42] It has also been reported in growth of 2D atomic layers and nanoribbons,[43–44] where gas-phase molecules continuously dissolve in the liquid catalyst until reaching saturation, thereby initiating and sustaining crystal nucleation and growth.[43] This represents the first demonstration that halide perovskite single-crystal wafers can be grown via the VLS pathway without any additional catalyst.

VLS growth mechanism for perovskite single-crystal wafer

To understand the control mechanism in perovskite single-crystal wafer VLS growth, reactions were quenched by stopping at the target temperature and rapidly cooling to room temperature to avoid side reactions during slow cooling. Subsequently, products were observed under SEM; films also presented curved edges (Fig. 3a), consistent with in situ observations and indicating that the in-situ reactor closely simulates tube furnace conditions. Simultaneously, continuous, uniform condensate appeared at film edges, corresponding to the liquid-phase region observed at high temperatures. Internal microstructure

of the solid–liquid interface (boxed region in Fig. 3a) was characterized by STEM. As shown, clear atomic arrangements in the film indicate good crystallinity, with no crystalline substances found in the liquid region (Fig. 3b). Corresponding selected-area electron diffraction (SAED) confirmed this: region I in Fig. 3b is amorphous, whereas regions II–IV all exhibit high single-crystal quality (Fig. 3c). Meanwhile, angle variations between lattice points (from 87° to 88°) suggest incomplete phase transition within the crystal. These results indicate that the liquid-phase region plays a crucial role in film growth.

To further clarify its composition, X-ray photoelectron spectroscopy (XPS) of quenched samples was performed. Br 3d shows a peak corresponding to zero-valent elemental bromine in addition to halide (Fig. 3d), whereas both Cs 3d and Pb 4f exhibit valence states characteristic of halide compounds (Supplementary Fig. S9). This derives from metal halide decomposition; metal elements also remain in the crucible (Supplementary Fig. S9). Notably, the critical temperature of pure bromine is below 315°C according to thermodynamic phase diagrams;[45] the bromine component observed at high temperatures arises from the general solution characteristic that boiling point elevation occurs due to metal halide mixing (Supplementary Note 1). TEM mapping in Fig. 3b indicates that Cs, Pb, and Br are distributed throughout the entire region, with Br presenting significantly stronger signals, indicating higher content (Fig. 3e). Corresponding line-scan profiles confirm this (Fig. 3f). Additionally, Raman spectra were acquired separately for liquid- and solid-phase regions (marked X and Y in Fig. 3g inset). Peaks at 75, 152, and 309 cm^{-1} correspond to rotational vibration of $[PbBr_6]^{4-}$ octahedra, asymmetric Br–Pb–Br stretching vibration, and symmetric Pb–Br bond stretching, respectively.[46] Rotational vibration of $[PbBr_6]^{4-}$ octahedra and Br–Pb–Br stretching (~ 141 cm^{-1}) are also observed in the liquid-phase region, indicating abundant $[PbBr_6]^{4-}$ octahedra (Fig. 3g).

Based on in situ observations and solid–liquid region compositional analysis, the VLS growth mechanism can be summarized (as illustrated in Fig. 4a). As metal halide precursors are heated and melted in the crucible, some decompose: $2CsBr \rightarrow 2Cs + Br_2\uparrow$; $PbBr_2 \rightarrow Pb + Br_2\uparrow$. These bromides evaporate together with metal halide precursors onto the substrate surface. Due to negligible temperature differences between vapor and substrate, commonly observed undercooling-driven crystallization does not occur. This enables vapor adsorption onto the substrate, followed by condensation into droplets once saturated vapor pressure is reached. As $PbBr_2$ and CsBr continuously evaporate and dissolve into the liquid phase, the solution gradually reaches saturation, whereupon nucleation and crystallization occur (Fig. 4a).

Furthermore, nucleation and growth of perovskite single-crystal films are co-determined by precursor supersaturation, substrate surface wettability, and surface diffusion length—low supersaturation, high wettability, and long diffusion length are desired (Supplementary Note 2). In the VLS pathway, the liquid-phase medium provides complete surface wetting, allowing precursors to move freely within the liquid phase without overcoming substrate lattice potential barriers (Fig. 4b, c), thereby effectively extending diffusion length. Meanwhile, supersaturation within the liquid phase is determined by the equilibrium between gas-phase dissolution and solid-phase growth and can be dynamically adjusted by liquid-phase volume changes, maintaining relatively constant levels (Supplementary Note 1). Consequently, statistics

from multiple substrate regions show significantly decreased nucleation density (three orders of magnitude lower than vapor–solid (VS) growth) (Fig. 4d, Supplementary Fig. S10), while effectively avoiding phenomena such as secondary nucleation. These results indicate that the VLS pathway offers substantial advantages for growing large-area halide perovskite single crystals.

All-inorganic halide perovskites exhibit tunable optoelectronic properties crucial for fabricating full-color light-emitting devices, broadband sensors, and other optoelectronic platforms. To verify scalability of the VLS approach, we successfully produced three additional single-crystal perovskite wafer compositions: $CsPbCl_3$, $CsPbCl_2Br$, and $CsPbClBr_2$, corresponding to complete and partial alloying at the halogen site. Photographs show color variations from white to yellow to brown as halogen composition transitions from chlorine to bromine (Fig. 4e–g), consistent with decreasing bandgap.[31] All wafers exhibit excellent uniformity and continuity across the entire wafer area, demonstrating the generality of the VLS method for fabricating single-crystal wafers with different all-inorganic perovskite compositions. Furthermore, XRD patterns exhibit sharp (100) and (200) diffraction peaks that gradually shift to lower angles with increasing atomic radius and lattice constant (Supplementary Fig. S11).

Optoelectronic properties of perovskite single-crystal wafers

To evaluate optoelectronic quality, femtosecond transient absorption (TA) spectroscopy was performed on $CsPbBr_3$ single-crystal wafers. The 2D contour TA map (Fig. 5a) displays well-resolved spectral features with clear temporal separation of ground-state bleach (GSB, negative blue signal below 530 nm) and broad excited-state absorption (ESA, positive red signal spanning 530–800 nm). The absence of severe spectral broadening or disorder-induced overlapping bands is characteristic of low structural disorder and minimized grain-boundary defects in single-crystal specimens. Time-resolved TA spectra at representative delay times (Fig. 5b) further reveal distinct band-edge GSB centered at 490–520 nm and stepwise decaying ESA bands at longer wavelengths. The sharp, symmetric GSB valley at the bandgap energy (~ 2.3 eV, 521 nm) confirms uniform band-edge electronic structure free from energetic disorder.

Normalized TA decay traces probed at 490, 520, 550, and 700 nm (Fig. 5c, Supplementary Note 3) reveal multi-timescale carrier relaxation without ultrafast defect quenching. Band-edge ESA at 520 nm exhibits a dominant sub-5 ps hot-carrier cooling component originating from weak electron–phonon coupling in the single-crystal lattice. Medium-lived (20–130 ps) decay channels correspond to intrinsic exciton dissociation and radiative bimolecular recombination. Minor nanosecond-scale slow components arise from weak shallow trap populations, whereas negligible amplitude of long-lived deep-trap species demonstrates drastically suppressed nonradiative recombination. The single-crystal film sustains persistent photoinduced carrier populations up to 3,000 ps. Collectively, the well-defined TA spectral profiles, ultrafast hot-carrier thermalization, and low trap-state densities indicate high crystallinity, low energetic disorder, and outstanding carrier transport performance.

Carrier transport performance was evaluated via the space-charge-limited current (SCLC) method using Au/$CsPbBr_3$/Au planar devices. Current–voltage (I–V) curves present three distinct regions

(Supplementary Fig. S12, Note 4). Carrier mobility and trap density (n_{trap}) were calculated to be 58.6 $cm^2 V^{-1} s^{-1}$ and 1.77×10^{10} cm^{-3}, respectively, indicating excellent electronic quality. Furthermore, photoelectronic response performance was investigated using the same devices (Fig. 5d) under 488-nm illumination at 4 mW cm^{-2}. Recorded dark current is ~ 10^{-9} A, whereas photocurrent reaches 10^{-6} A, corresponding to a high on/off ratio of 10^3—superior to VS-grown film devices. Meanwhile, responsivity shows good linear dependence on light intensity, with maximum responsivity exceeding 10^4, demonstrating excellent photoconductivity (Fig. 5e). Notably, device rise and fall times were 0.74 μs and 1.2 μs, respectively—significantly faster than reference VS-grown film devices (5.6 μs and 11.5 μs) (Fig. 5f). These results collectively indicate that VLS-grown films exhibit superior optoelectronic properties.

Conclusion

In summary, we have demonstrated catalyst-free VLS growth of 2-inch perovskite single-crystal wafers. A condensed halide-rich liquid intermediate creates complete surface wetting and replaces high-energy vapor–solid interfaces with low-energy vapor–liquid and liquid–solid interfaces, substantially reducing both nucleation energy barriers and nucleation density. The liquid-phase medium also dramatically extends metal halide solute migration distances, enabling edge-dominated layer growth and seamless coalescence of oriented nuclei. We further fabricated wafer-scale films of $CsPbBr_3$, $CsPbCl_3$, and their alloys, demonstrating the scalability of this strategy. Atomic-scale microscopy and wafer-scale spectroscopy confirm exceptional crystalline uniformity, ultralow trap-state density, and superior electronic and optoelectronic quality. The VLS paradigm overcomes fundamental vapor-growth limitations, providing a viable route toward scalable manufacturing of high-performance perovskite single-crystal devices.

Methods

Growth of $CsPbX_3$ perovskite single crystal wafers

VLS growth of $CsPbX_3$ single-crystal films was performed via modified chemical vapor deposition. First, 2-inch sapphire substrates were ultrasonically cleaned three times with isopropanol, acetone, and deionized water. Then, 0.5 mmol CsBr (99.5%, Aladdin) and 1.0 mmol $PbBr_2$ (99.5%, Aladdin) were mixed and placed in an alumina crucible (diameter 3 cm). The sapphire substrate was placed on top of the crucible, which was subsequently positioned at the center of the tube furnace. Internal atmosphere was maintained at 50 Pa, followed by heating to 510°C at 2°C min^{-1}. After holding for 10 minutes, continuous, uniform large-area $CsPbBr_3$ films were grown on the substrate. Growth on mica substrates followed the same procedure, with care taken to keep freshly cleaved mica substrates flat and clean.

For growth of single-crystal $CsPbCl_3$, $CsPbCl_2Br$, and $CsPbClBr_2$ wafers, experimental conditions were kept identical to those for $CsPbBr_3$ except for metal halide precursors and deposition temperature. Specifically, metal halide salts were replaced with corresponding counterparts, and deposition

temperatures were adjusted to 530°C, 520°C, and 515°C for $CsPbCl_3$, $CsPbCl_2Br$, and $CsPbClBr_2$, respectively.

Reference VS-grown $CsPbBr_3$ single-crystal films were prepared as follows. Sapphire substrates were ultrasonically cleaned three times with isopropanol, acetone, and deionized water. Then, 0.5 mmol CsBr and 1.0 mmol $PbBr_2$ were mixed, placed in a crucible, and positioned at the center of the tube furnace. The sapphire substrate was placed downstream (6 cm from the crucible). High-purity argon gas was used to eliminate oxygen and moisture (three purge cycles). During growth, Ar flow rate was set at 100 sccm at 104 Pa. The furnace was ramped to 550°C and held for 10 min, depositing $CsPbBr_3$ single-crystal films.

Characterizations

Optical microscopy images were acquired using a Nikon ECLIPSE LV150N microscope. Atomic force microscopy was performed with a Bruker Dimension Icon. Scanning electron microscopy images were captured with a Hitachi SU-8010. Electron backscatter diffraction was collected using an Oxford Nordlys Max³. Transmission electron microscopy and scanning transmission electron microscopy were performed using a Tecnai F20 operated at 80 kV equipped with X-ray energy-dispersive spectroscopy. X-ray diffraction patterns, including φ-scans and rocking curves, were measured using a Bruker D8 Advance X-ray diffractometer. In situ visual CVD observations were performed using a JYR1000DEP (UNITS). Transient absorption spectra were acquired with a PhysTech FT1230 HERA system. X-ray photoelectron spectroscopy was performed with a Thermo Fisher Scientific ESCALAB XI^+. Raman spectra were acquired with a HORIBA LabRAM Odyssey. Photographs were taken with a HUAWEI Pura 90 Pro Max (50 megapixels).

Device Fabrication and Characterization

Devices for SCLC measurements and photodetectors used an Au/perovskite/Au planar structure. A 100-nm-thick Au layer was deposited on the perovskite surface through a mask with 10-μm channel spacing and 200-μm width. Electrical and photoelectrical measurements were performed on a probe station (Lakeshore TTP4) equipped with a semiconductor parameter analyzer (Keithley 4200). A 488-nm laser was used as the illumination source.

Declarations

Data availability

The source data underlying Figs. 1–5 and Supplementary Figs. S1–S12 are provided with this paper. Additional information is available from the corresponding authors on reasonable request.

Additional information

Competing interests:

The authors declare no competing interests.

Author contributions

This work was contributions from all authors. Y. Chen, H. Wang, and G. Zou conceived the idea, supervised the whole project, and co-wrote the manuscript. Y. Chen, G. Hu, W. Zhang, and Y. Wang conducted the mainly experiments, characterizations, and analyzed the data. J. Cao and H. Shi contributions on the in-situ growth characterization and data analysis. J. Chen, H. Wang, G. Zhao and S. Cong contributions on STEM and device characterizations. C. Wang and P. Ma provided the transient absorption characterization and data analysis. All authors have commented on the manuscript.

Acknowledgements

We gratefully acknowledge the National Natural Science Foundation of China (52325309, 22488101), the National Key R&D Program of China (2024YFA1509300), Guangdong S&T Program (2026B0101070005), the Natural Science Foundation of Shandong Province (ZR2024QF273), GBRCE for Functional Molecular Engineering and Institute of Green Chemistry and Molecular Engineering, the Gusu Innovation and Entrepreneurship Leading Talent Program (ZXL2024383), the Natural Science Foundation of the Jiangsu Higher Education Institution of China (No. 22KJA430013), and the Key Lab of Advanced Optical Manufacturing Technologies of Jiangsu Province & Key Lab of Modern Optical Technologies of Ministry of Education.

References

1. Wang Y, Wu T, Barbaud J, Kong W, Cui D, Chen H, Yang X, Han L (2019) Stabilizing heterostructures of soft perovskite semiconductors. Science 365:687–691
2. Jiang Q, Tong J, Scheidt RA, Wang X, Louks AE, Xian Y, Tirawat R, Palmstrom AF, Hautzinger MP, Harvey SP, Johnston S, Schelhas LT, Larson BW, Warren EL, Beard MC, Berry JJ, Yan Y (2022) Zhu. Compositional texture engineering for highly stable wide-bandgap perovskite solar cells. Science 378:1295–1300
3. Xu J, Boyd CC, Yu ZJ, Palmstrom AF, Witter DJ, Larson BW, France RM, Werner J, Harvey SP, Wolf EJ, Weigand W, Manzoor S, Berry MF, Luther JM (2020) Z. C. Holman; M. D. McGehee. Triple-halide wide–band gap perovskites with suppressed phase segregation for efficient tandems. *Science 367*: 1097–1104
4. Dong Y, Wang YK, Yuan F, Johnston A, Liu Y, Ma D, Choi MJ, Chen B, Chekini M, Baek SW, Sagar LK, Fan J, Hou Y, Wu M, Lee S, Sun B, Hoogland S, Quintero-Bermudez R, Ebe H, Todorovic P, Dinic F, Li P, Kung HT, Spiecker E, Liao LS, Voznyy O, Lu ZH (2020) Sargent. Bipolar-shell resurfacing for blue

LEDs based on strongly confined perovskite quantum dots. Nat Nanotech 15:668–674 M. I. Saidaminov; E. Kumacheva

5. Min H, Wang N, Chen N, Tong Y, Wang Y, Wang J, Liu J, Wang S, Wu X, Yang P, Shi H, Zhuo C, Chen Q, Li J, Zhang D, Lu X, Zhu C, Peng Q, Zhu L, Chang J, Huang W (2024) Wang. Spin coating epitaxial heterodimensional tin perovskites for light-emitting diodes. Nat Nanotech 19:632–637
6. Yuan F, Folpini G, Liu T, Singh U, Treglia A, Lim JWM, Klarbring J, Simak SI, Abrikosov IA, Sum TC, Petrozza A (2024) Gao. Bright and stable near-infrared lead-free perovskite light-emitting diodes. Nat Photonics 18:170–176
7. Qin C, Sandanayaka ASD, Zhao C, Matsushima T, Zhang D, Fujihara T (2020) Adachi. Stable room-temperature continuous-wave lasing in quasi-2D perovskite films. Nature 585:53–57
8. Zhu H, Fu Y, Meng F, Wu X, Gong Z, Ding Q, Gustafsson MV, Trinh MT, Jin S (2015) Zhu. Lead halide perovskite nanowire lasers with low lasing thresholds and high quality factors. Nat Mater 14:636–642
9. Yakunin S, Sytnyk M, Kriegner D, Shrestha S, Richter M, Matt GJ, Azimi H, Brabec CJ, Stangl J, Kovalenko MV (2015) Heiss. Detection of X-ray photons by solution-processed organic-inorganic perovskites. Nat Photonics 9:444–449
10. Dou L, Yang YM, You J, Hong Z, Chang WH, Li G, Yang Y (2014) Solution-processed hybrid perovskite photodetectors with high detectivity. Nat Commun 5:5404–5410
11. Zhuang R, Wang X, Ma W, Wu Y, Chen X, Tang L, Zhu H, Liu J, Wu L, Zhou W, Liu X (2019) Yang. Highly sensitive X-ray detector made of layered perovskite-like (NH4)3Bi2I9 single crystal with anisotropic response. Nat Photonics 13:602–608
12. Chen Q, Wu J, Ou X, Huang B, Almutlaq J, Zhumekenov AA, Guan X, Han S, Liang L, Yi Z, Li J, Xie X, Wang Y, Li Y, Fan D, Teh DBL; A. H., Liu X (2018) All-inorganic perovskite nanocrystal scintillators. Nature 561:88–93 All; O. F. Mohammed; O. M. Bakr; T. Wu; M. Bettinelli; H. Yang; W. Huang
13. Wang L, Zhou H, Hu J, Huang B, Sun M, Dong B, Zheng G, Huang Y, Chen Y, Li L, Xu Z, Li N, Liu Z, Chen Q, Sun L-D (2019) Yan. A Eu3+-Eu2 + ion redox shuttle imparts operational durability to Pb-I perovskite solar cells. Science 363:265–270
14. Lin Y, Chen B, Fang Y, Zhao J, Bao C, Yu Z, Deng Y, Rudd PN, Yan Y, Yuan Y (2018) Huang. Excess charge-carrier induced instability of hybrid perovskites. Nat Commun 9:4981
15. Lei Y, Chen Y, Xu S (2021) Single-crystal halide perovskites: Opportunities and challenges. Matter 4:2266–2308
16. Li C, Sun H, Gan S, Dou D, Li L (2023) Perovskite single crystals: physical properties and optoelectronic applications. *Mater. Futur. 2*
17. Liu N, Liu M, Dai J, Cheng X, Chen Z (2025) Nucleation Engineering to Strengthen Interface Contacts in Single-Crystal Perovskite Photovoltaics. Angew Chem 64:e202500947
18. Yuan M, Feng J, Li H, Gao H, Qiu Y, Jiang L (2025) Wu. Remote epitaxial crystalline perovskites for ultrahigh-resolution micro-LED displays. Nat Nanotech 20:381–387

19. Wenjing ZH, Chen H, Yao Y, Liu Y, Zhang HZ, Zhijian Li P, Xiao T, Chen (2022) Haiding Sun, Jinsong Huang, Zhengguo Xiao. Highly bright and stable single-crystal perovskite light-emitting diodes. Nat Photonics 17:401–407
20. Li T, Guo W, Ma L, Li W, Yu Z, Han Z, Gao S, Liu L, Fan D, Wang Z, Yang Y, Lin W, Luo Z, Chen X, Dai N, Tu X, Pan D, Yao Y, Wang P, Nie Y, Wang J, Shi Y (2021) X. Wang. Epitaxial growth of wafer-scale molybdenum disulfide semiconductor single crystals on sapphire. Nat Nanotech 16:1201–1207
21. Yamamura A, Watanabe S, Uno M, Mitani M, Mitsui C, Tsurumi J, Isahaya N, Kanaoka Y, Okamoto T, Takeya J (2018) Wafer-scale, layer-controlled organic single crystals for high-speed circuit operation. Sci Adv 4:eaao5758
22. Lee L, Baek J, Park KS, Lee YE, Shrestha NK (2017) Sung. Wafer-scale single-crystal perovskite patterned thin films based on geometrically-confined lateral crystal growth. Nat Commun 8:15882
23. Xu X, Pan Y, Liu S, Han B, Gu P, Li S, Xu W, Peng Y, Han Z, Chen J, Gao P, Ye Y (2021) Seeded 2D epitaxy of large-area single-crystal films of the van der Waals semiconductor 2H MoTe2. Science 372:195–200
24. Chen YX, Ge QQ, Shi Y, Liu J, Xue DJ, Ma JY, Ding J, Yan HJ, Hu JS (2016) Wan. General Space-Confined On-Substrate Fabrication of Thickness-Adjustable Hybrid Perovskite Single-Crystalline Thin Films. J Am Chem Soc 138:16196–16199
25. Chen Z, Dong Q, Liu Y, Bao C, Fang Y, Lin Y, Tang S, Wang Q, Xiao X, Bai Y, Deng Y (2017) Huang. Thin single crystal perovskite solar cells to harvest below-bandgap light absorption. Nat Commun 8:1890–1897
26. Liu D, Zheng Y, Sui XY, Wu XF, Zou C, Peng Y, Liu X, Lin M, Wei Z, Zhou H, Yao Y-F, Dai S, Yuan H, Yang HG, Yang S (2024) Y. Hou. Universal growth ofperovskite thin monocrystals from high solute flux for sensitive self-driven X-ray detection. Nat Commun 15:2390
27. Lei YS, Chen YM, Zhang RQ, Li YH, Yan QZ, Lee S, Yu YG, Tsai H, Choi W, Wang KP, Luo YQ, Gu Y, Zheng XR, Wang CF, Wang CH, Hu HJ, Li Y, Qi BY, Lin MY, Zhang ZR, Dayeh SA, Pharr M, Fenning DP, Lo YH; J. Luo;, Yang KS, Yoo J (2020) W. Y. Nie; S. Xu. A fabrication process for flexible single-crystal perovskite devices. *Nature 583*: 790–795
28. Lei Y, Chen Y, Gu Y, Wang C, Huang Z, Qian H, Nie J, Hollett G, Choi W, Yu Y, Kim N, Wang C, Zhang T, Hu H, Zhang Y, Li X, Li Y, Shi W, Liu Z, Sailor MJ, Dong L, Lo Y-H (2018) J. Luo; S. Xu. Controlled Homoepitaxial Growth of Hybrid Perovskites. *Adv. Mater. 30*: 1705992
29. Chen J, Morrow DJ, Fu Y, Zheng W, Zhao Y, Dang L, Stolt MJ, Kohler DD, Wang X, Czech KJ, Hautzinger MP, Shen S, Guo L, Pan A, Wright JC (2017) Jin. Single-Crystal Thin Films of Cesium Lead Bromide Perovskite Epitaxially Grown on Metal Oxide Perovskite (SrTiO3). J Am Chem Soc 139:13525–13532
30. Wang Y, Sun X, Chen Z, Sun YY, Zhang S, Lu TM, Wertz E (2017) Shi. High-Temperature Ionic Epitaxy of Halide Perovskite Thin Film and the Hidden Carrier Dynamics. Adv Mater 29:1702643–1702651
31. Lin X, Chen L, He C, Wang Y, Li X, Dang W, He K, Huangfu Y, Wu D, Zhao B, Li B, Li J (2022) Duan. Vapor Phase Growth of Centimeter-Sized Band Gap Engineered Cesium Lead Halide Perovskite

Single-Crystal Thin Films with Color-tunable Stimulated Emission. Adv Funct Mater 33:2210278

32. Kim H, Lee S, Shin J, Zhu M, Akl M, Lu K, Han NM, Baek Y, Chang CS, Suh JM, Kim KS, Park BI, Zhang Y, Choi C, Shin H, Yu H, Meng Y, Kim SI, Seo S, Lee K, Kum HS, Lee JH, Ahn JH, Bae SH, Hwang J, Shi Y (2022) J. Kim. Graphene nanopattern as a universal epitaxy platform for single-crystal membrane production and defect reduction. Nat Nanotech 17:1054–1059
33. Wang Y, Yang F, Li X, Ru F, Liu P, Wang L, Ji W, Xia J (2019) Meng. Epitaxial Growth of Large-Scale Orthorhombic CsPbBr3 Perovskite Thin Films with Anisotropic Photoresponse Property. Adv Funct Mater 29:1904913
34. Nasyedkin K, King I, Zhang L, Chen P, Wang L, Staples RJ, Lunt RR (2021) Pollanen. Extraordinary phase coherence length in epitaxial halide perovskites. iScience 24:102912
35. Zhao L, Gao Y, Su M, Shang Q, Liu Z, Li Q, Wei Q, Li M, Fu L, Zhong Y, Shi J, Chen J, Zhao Y, Qiu X, Liu X, Tang N, Xing G, Wang X, Shen B (2019) Zhang. Vapor-Phase Incommensurate Heteroepitaxy of Oriented Single-Crystal CsPbBr3 on GaN: Toward Integrated Optoelectronic Applications. ACS Nano 13:10085–10094
36. Zhong Y, Liao K, Du W, Zhu J, Shang Q, Zhou F, Wu X, Sui X, Shi J, Yue S, Wang Q, Zhang Y, Zhang Q, Hu X (2020) Liu. Large-Scale Thin CsPbBr3 Single-Crystal Film Grown on Sapphire via Chemical Vapor Deposition: Toward Laser Array Application. ACS Nano 14:15605–15615
37. Liu C, Liu T, Zhang Z, Sun Z, Zhang G, Wang E (2024) Liu. Understanding epitaxial growth of two-dimensional materials and their homostructures. Nat Nanotech 19:907–918
38. Li X, Liu C, Ding F, Lu Z, Gao P, Huang Z, Dang W, Zhang L, Lin X, Ding S, Li B, Huangfu Y, Shen X, Li B, Zou X, Liu Y, Liao L, Wang Y (2023) Duan. Ultra-Stable and Sensitive Ultraviolet Photodetectors Based on Monocrystalline Perovskite Thin Films. Adv Funct Mater 33:2213360
39. Dong S, Huang J, Zhang F, Zhou W, Fu H (2026) Q. Zheng. Highly Oriented Inch-Scale Monocrystalline 0D/3D Perovskite Heterojunction Films via Vapor-Phase Epitaxy for Self-Powered Photodetectors. ACS Nano 20:10345–10357
40. Jiang H, Zhang X, Chen K, He X, Liu Y, Yu H, Gao L, Hong M, Wang Y, Zhang Z, Zhang Y (2025) Two-dimensional Czochralski growth of single-crystal MoS2. Nat Mater 24:188–196
41. Meng Y, Lan C, Li F, Yip S, Wei R, Kang X, Bu X, Dong R, Zhang H (2019) Ho. Direct Vapor-Liquid-Solid Synthesis of All-Inorganic Perovskite Nanowires for High-Performance Electronics and Optoelectronics. ACS Nano 13:6060–6070
42. Meyers JK, Kim S, Hill DJ, Cating EEM, Williams LJ, Kumbhar AS, McBride JR, Papanikolas JM (2017) Cahoon. Self-Catalyzed Vapor-Liquid-Solid Growth of Lead Halide Nanowires and Conversion to Hybrid Perovskites. Nano Lett 17:7561–7568
43. Li S, Lin Y-C, Zhao W, Wu J, Wang Z, Hu Z, Shen Y, Tang D-M, Wang J, Zhang Q, Zhu H, Chu L, Zhao W, Liu C, Sun Z, Taniguchi T, Osada M, Chen W, Xu Q-H, Wee ATS, Suenaga K, Ding F, Eda G (2018) Vapour–liquid–solid growth of monolayer MoS2 nanoribbons. Nat Mater 17:535–542
44. Chang M-C, Ho P-H, Tseng M-F, Lin F-Y, Hou C-H, Lin IK, Wang H, Huang P-P, Chiang C-H, Yang Y-C, Wang IT, Du H-Y, Wen C-Y, Shyue J-J, Chen C-W, Chen K-H, Chiu P-W (2020) Chen. Fast growth of

large-grain and continuous MoS2 films through a self-capping vapor-liquid-solid method. Nat Commun 11:3682

45. Acree WEJC (2026) J. S. Phase Transition Enthalpy Measurements of Organic and Organometallic Compounds, in *NIST Chemistry WebBook, Vol. 69*, National Institute of Standards and Technology Database. https://doi.org/10.18434/T4D303

46. Iaru CM, Brodu A, van Hoof NJJ, Ter Huurne SET, Buhot J, Montanarella F, Buhbut S, Christianen PCM, Vanmaekelbergh D, de Donega C, Rivas JG, Koenraad PM (2021) A. Y. Silov. Frohlich interaction dominated by a single phonon mode in CsPbBr3. *Nat. Commun. 12*: 5844

Figures

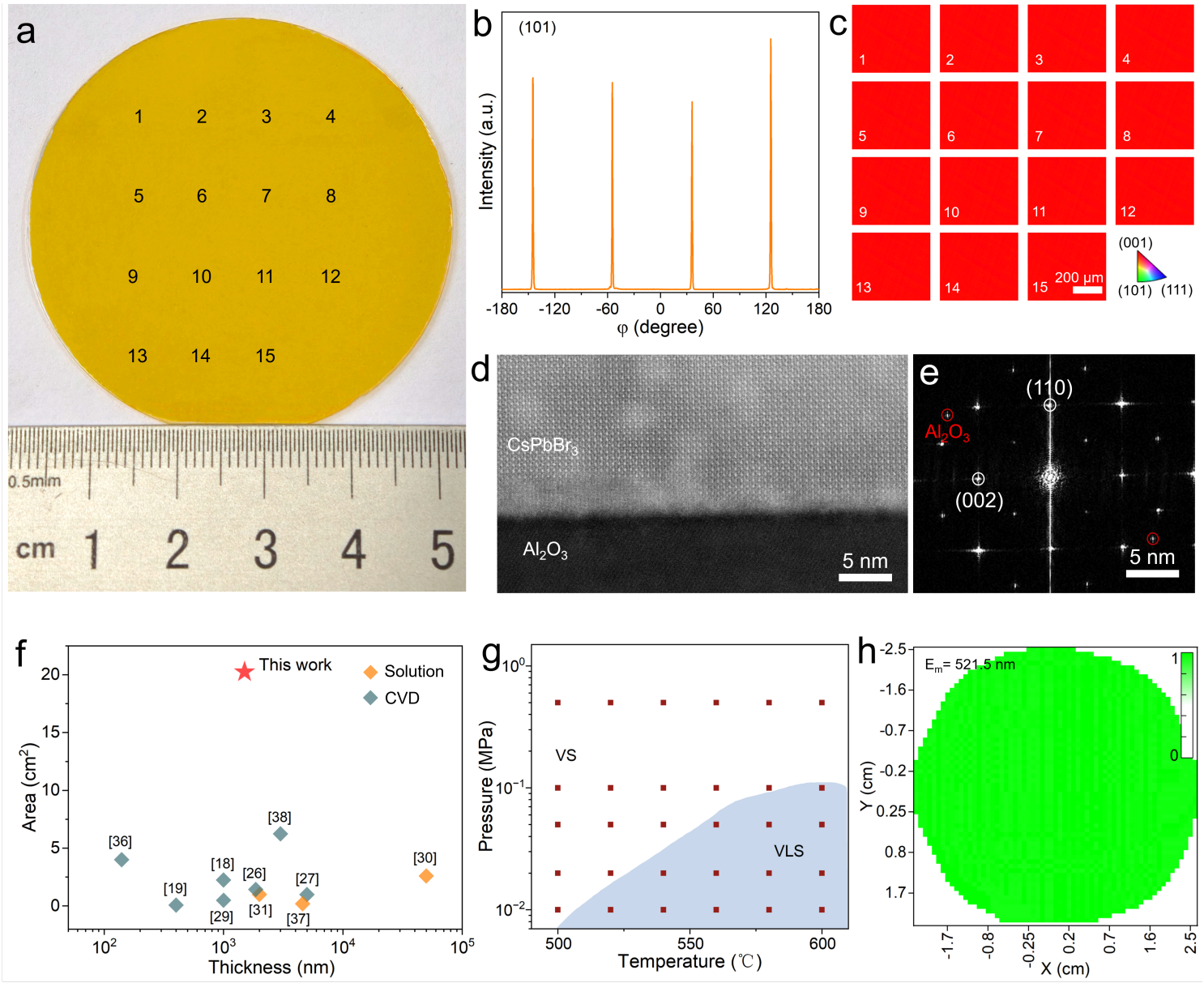


Figure 1

Morphology and microstructure of the synthetic $CsPbBr_3$ perovskite wafer. (a) Digital camera photograph of the $CsPbBr_3$ wafer on sapphire substrate. (b) in-plan XRD Phi-scan of the $CsPbBr_3$ wafer. (c) EBSD images of the $CsPbBr_3$ wafer that was collected from the marked fifteen region of (a) with the area of 600×600 μm^2. (d) cross-sectional STEM image of the $CsPbBr_3$ wafer. (e) The corresponding FFT image of the (d). (f) The statistics and comparison of the representative size and thickness of perovskite single-crystal thin films prepared in the literature and this work, where the orange represents the solution method, and indigo represents the vapor deposition method. (g) The preferred growth map of VLS at the ranged reaction temperature (490~610 ℃) and pressure (0.007~0.5 MPa). (h) PL intensity mapping image across the whole perovskite wafer, with the emission center at 521.5 nm.

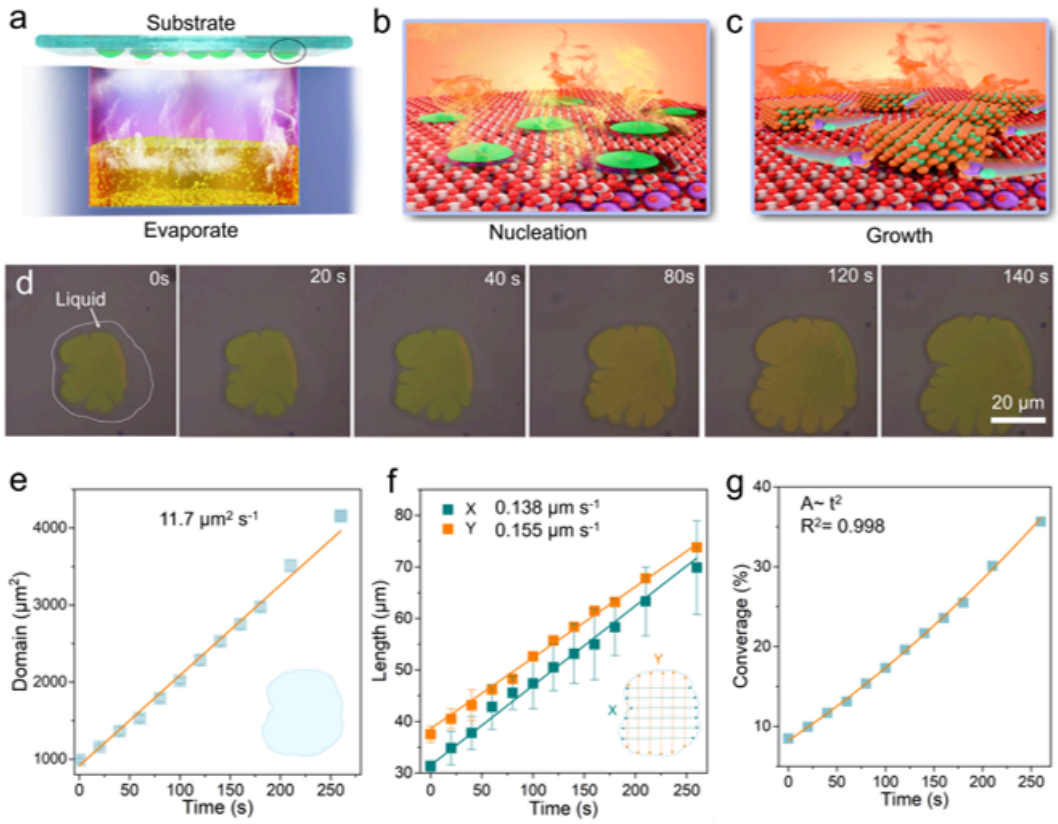


Figure 2. In situ growth observation of $CsPbBr_3$ perovskite single crystal film. (a) illustration of substrate placement position and precursor transport direction during the growth process. (b, c) illustration of nucleation and growth for perovskite single crystal wafer. (d) The instantaneous slice images of during high-temperature in-situ growth stage for perovskite single crystal film, where the process was holding 140 seconds. (e) Statistics of domain size evolution over time, the fitting model between holding time and domain size was: $D(t) = 0.012t^2 + 9t + 965$. (f) Statistics of horizontal/vertical size evolution over time, the fitting model between holding time and horizontal/vertical size was: $X(t) = 0.138t + 31.5$, $Y(t) = 0.155t + 38.6$. (g) Statistics and fitting of coverage evolution over time, the fitting model between holding time and coverage was: $C(t) = t^2 + 0.08t + 8.2$.

Figure 2

See image above for figure legend.

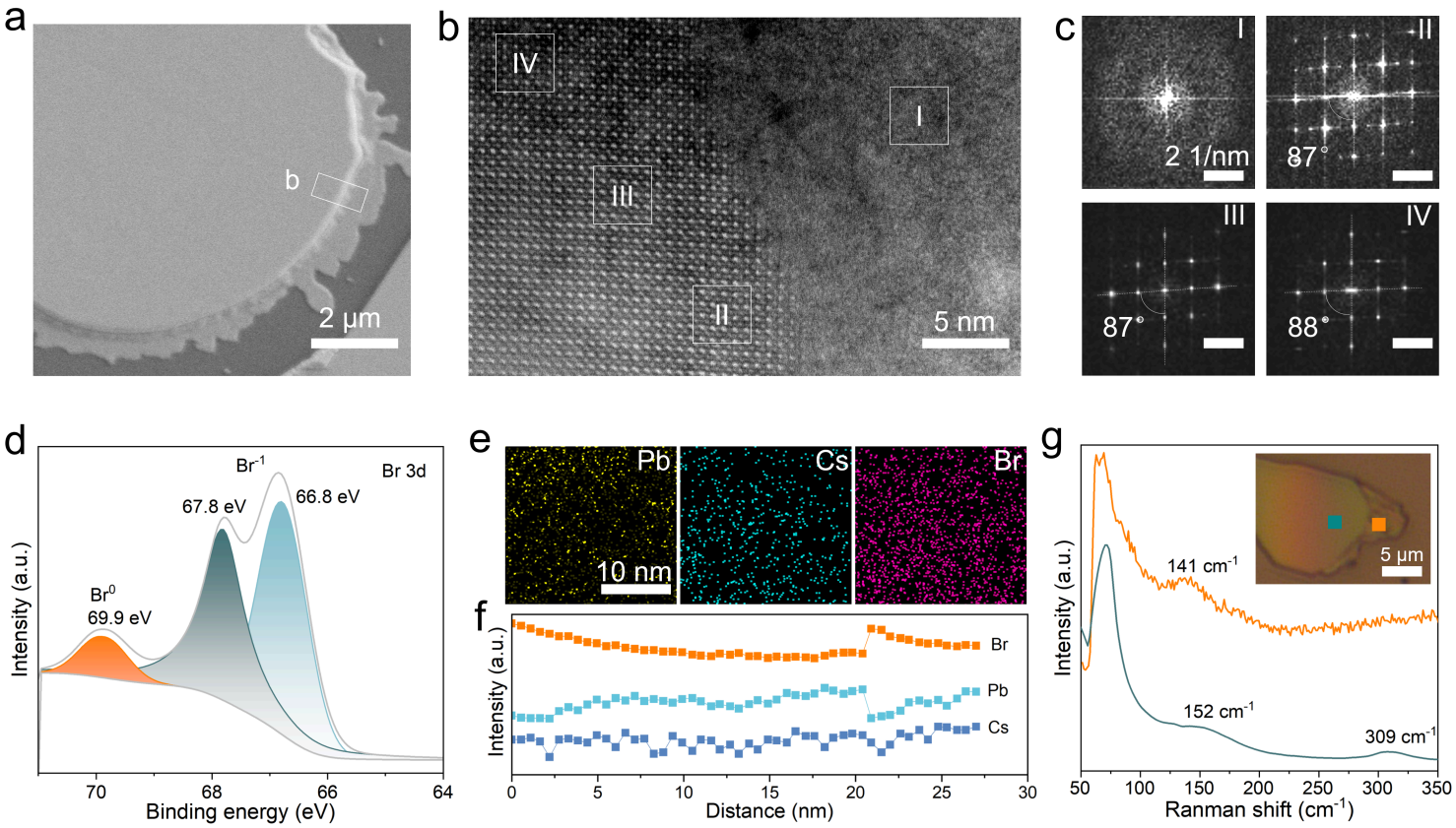


Figure 3

Composition characterizations of the liquid-solid interface region. (a) SEM image of the film crystal edge that was quickly quenched during the growth process. (b) The STEM image of the liquid-solid interface. (c) The FFT images of the liquid-solid interface with the marked four regions in (b). (d) The Br 3d XPS high-resolution spectra of the quenched crystal. (e, f) The EDS mapping image and line spectra of the liquid-solid interface. (g) The Raman spectra of the liquid phase and solid phase that marked in the insert.

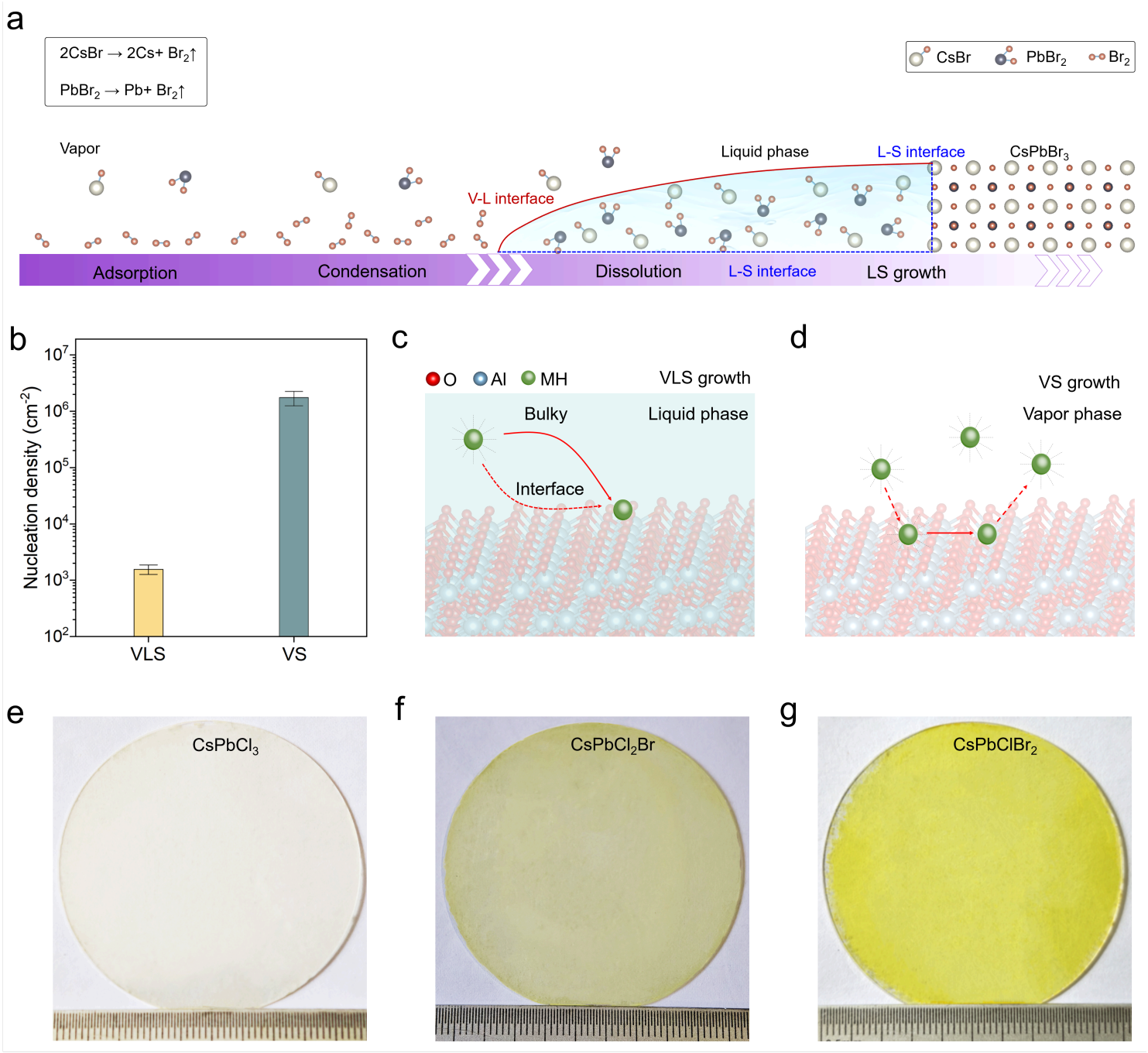


Figure 4

Growth mechanism and scalability of perovskite single crystal wafer through VLS pathway. (a) Schematic diagram of vapor-liquid-solid growth mechanism that is composed of precursor decomposition, adsorption by substrate, condensation, precursor dissolution, and liquid-solid growth, respectively. (b) Nucleation density statistics of VLS and VS. (c, d) Schematic diagram of volume diffusion and interfacial diffusion of precursor molecules during VLS and VS growth pathway. (e-g) The digital camera photos of 2-inch sized $CsPbCl_3$, $CsPbCl_2Br$, and $CsPbClBr_2$ that grown through VLS method.

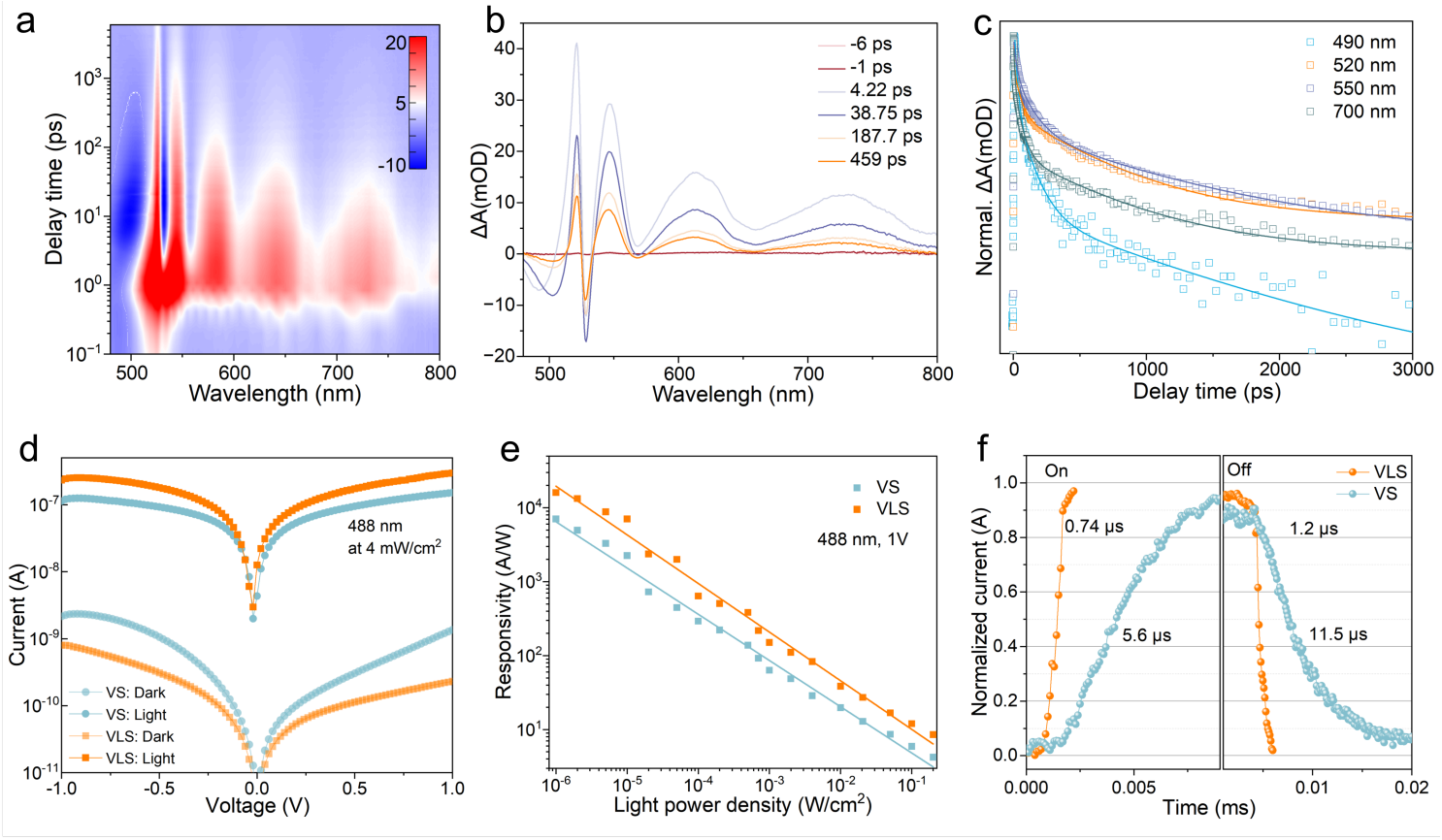


Figure 5

Optoelectronic properties of $CsPbBr_3$ perovskite single crystal wafers. (a) 2D contour plot of transient absorption spectra for single-crystalline $CsPbBr_3$ thin film. (b) Representative transient absorption spectra recorded at typical delay times. (c) Normalized kinetic decay curves monitored at 490, 520, 550, and 700 nm. (d) The current-voltage curve of the perovskite wafer in light/dark state, with excitation wavelength of 488 nanometers and intensity of 0.5 mW cm^{-2}. (e) The device responsivity of VLS and VS single-crystal films under various light intensities. (f) The device response speed of VLS and VS grown single-crystal films.

Supplementary Files

This is a list of supplementary files associated with this preprint. Click to download.

- Supportinginformation.docx
- VideoS1.mp4